Extended windage loss models for gas bearing supported spindles operated in dense gases

Kévin Rosset*, Jürg Schiffmann

kevin.rosset@epfl.ch, jurg.schiffmann@epfl.ch

Ecole Polytechnique Fédérale de Lausanne (EPFL),
Laboratory for Applied Mechanical Design (LAMD),
Rue de la Maladière 71b, 2002 Neuchâtel, Switzerland

* Corresponding Author

ABSTRACT

Generic models are proposed to evaluate the skin friction coefficient acting on enclosed rotating disks and cylinders under various flow regimes. In particular, a model taking into account the inner radius of the disk is developed. The models are compared with experimental data obtained from coast-down tests of a high-speed spindle supported on gas lubricated bearings, operated in air and in halocarbon R245fa at various pressures. The windage losses are first computed considering state of the art laminar flow loss models in the gas bearings and an experimentally validated laminar-turbulent flow loss model in the air-gap. This reference approach predicts the air data with a good accuracy (deviation less than 5%) but underestimates the organic fluid data by up to 36%. This deviation is considerably reduced (max 6.8%) when applying the proposed multi flow regime loss model for enclosed rotating disks to the thrust bearing. Finally, the proposed laminar-turbulent flow loss model for enclosed rotating cylinders is simultaneously applied to the journal bearings and the air-gap. A peak deviation of 6.5% is maintained among all test cases when setting the critical Taylor number to an artificial value (67) instead of the theoretical value (41.1) characterizing the onset of growth of Taylor vortices. Taking into account the uncertainties on the bearing clearances, as well as on the operating pressure and temperature, a ±10% agreement with the experimental data is obtained.

Keywords: windage, loss model, skin friction coefficient, enclosed rotating cylinder, enclosed rotating disk, laminar flow, turbulent flow, gas bearing, grooved bearing, air-gap, high-speed spindle, dense gas

1. Introduction

Due to their ability to achieve high rotational speeds and to operate without petroleum-based lubricant, gas-lubricated bearings are a convenient solution to support high-speed rotating machinery, while avoiding process fluid contamination. They are particularly suited for small-scale turbomachinery applications such as fuel cell air compressors [1], fuel cell anode off-gas recirculation fans [2,3], vapor compression cycle compressors [4,5], or organic Rankine cycle turbines [6]. Such bearings are subjected to viscous friction losses in the narrow clearance between the rotating and the stationary parts. These losses are typically predicted by assuming laminar Couette flow throughout the clearance [7,8]. However, depending on the clearance and the operating conditions (speed, fluid properties), flow instabilities may occur and cause a significant increase in friction losses. Applications using dense gases, such as vapor compression and organic Rankine cycles, are especially concerned. Furthermore, not only gas bearings are subjected to these so-called windage losses but also magnetic bearings [9,10], labyrinth seals [11], high-speed gears [12], and electrical machines [13–15]. When designing high-speed spindles, the accurate prediction of windage losses is critical in order to both maximize the efficiency and define an appropriate thermal management strategy.

1.1 Nature of the issues

While assessing the performance of a high-speed spindle supported on two herringbone-grooved journal bearings (HGJB) and a double-sided spiral-grooved thrust bearing (SGTB), the measured friction losses are in good agreement with the state of the art loss models [8,16] when operating the spindle in air. However, the model predictions significantly underestimate the measured losses when operating the spindle in a dense organic vapor (Figure 1). This mismatch suggests that the laminar flow assumption might not be applicable anymore and that more advanced loss models, taking into account turbulence, should be considered.

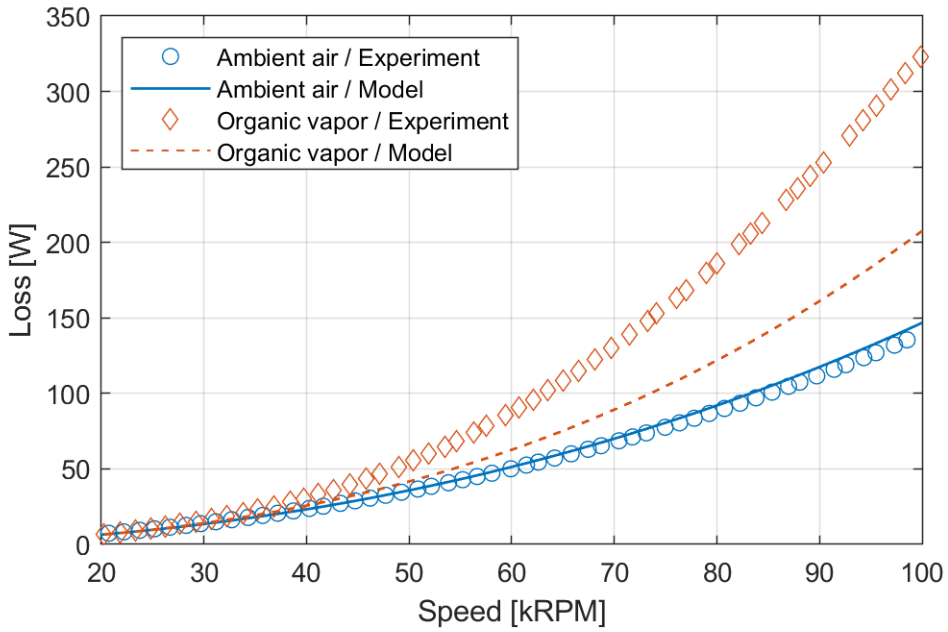

Figure 1: Comparison between the experimental friction loss of the spindle and the state of the art loss model. The experimental data were obtained through coast-down tests and the corresponding measurement procedure is described in section 2.4.2. The global loss model is detailed in section 2.4.3 while the state of the art version is discussed in section 3.2.1.

1.2 Goal and objectives

The goal of this study is an experimental validation of windage loss models for gas bearing supported spindles operated in dense gases. The objectives are (1) to review existing models, (2) to build generic models suitable for various flow regimes and (3) to validate the proposed models based on experimental data.

1.3 Scope of the paper

This paper is divided into two core sections. In section 2, theory and correlations for predicting the skin friction coefficient acting on rotating cylinder and disk are reviewed. New models taking into account various flow regimes are then proposed, and the combination of models used to predict the total losses of the investigated spindle are described. In section 3, reference and new models are compared with experimental data, and an uncertainty analysis is conducted in order to assess the effect of clearance, pressure and temperature on loss prediction. The effect of pressurization in the gas bearings is also investigated. Section 4 concludes on the validation of the new models.

2. Predictive models

2.1 Theory and laminar flow regime

The viscous friction loss P_f over a rotating body is the product of the viscous friction torque T_f and the angular speed ω of the rotating body:

$$P_f = \omega T_f \tag{1}$$

The viscous friction torque is evaluated by integrating the local shear stress τ_f acting on the surface of the body:

$$T_f = \int \tau_f r dA \tag{2}$$

From a global point of view, the viscous friction torque can also be expressed as a function of a global shear stress $\bar{\tau}_{f*}$ acting on the whole surface A of the body and associated to a reference radius r_*:

$$T_f = \bar{\tau}_{f*} r_* A \tag{3}$$

The global shear stress can be further expressed as the product of a non-dimensional skin friction coefficient C_f and a dynamic pressure p_*, which depends on the fluid density ρ and the reference tip speed:

$$\bar{\tau}_{f*} = C_f p_* = C_f \frac{1}{2} \rho (\omega r_*)^2 \tag{4}$$

In the following subsections, the skin friction coefficient associated with laminar flow over enclosed rotating cylinder and disk (Figure 2) is derived.

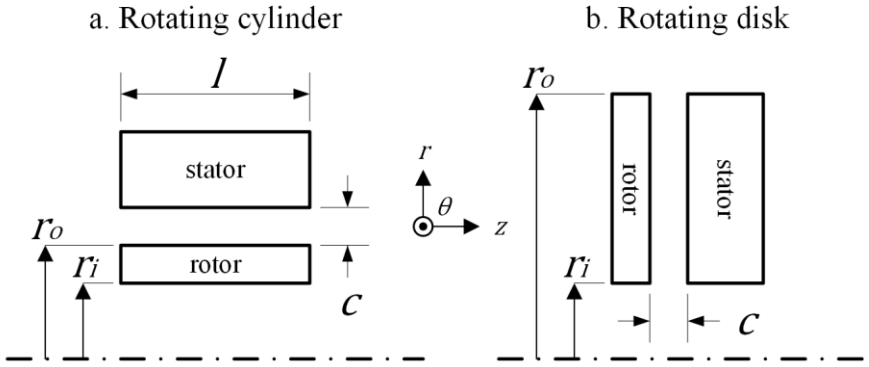

Figure 2: Cross-sectional view of basic enclosed rotating bodies

2.1.1 Rotating cylinder

In cylindrical coordinates, the local shear stress throughout the radially extended clearance from an enclosed rotating cylinder is defined as:

$$\tau_{r\theta} = \mu \left[\frac{1}{r} \frac{\partial v_r}{\partial \theta} + r \frac{\partial}{\partial r} \left(\frac{v_\theta}{r} \right) \right]$$

Considering the situation represented in Figure 2a, and assuming no radial flow and a linear velocity profile with no-slip boundary conditions (Couette flow) in the tangential direction (Equation 5), the local shear stress acting on the surface of the cylinder reduces to Equation 6.

$$v_\theta(r) = \frac{\omega r_o}{c} (r - c - r_o) \tag{5}$$

$$\tau_f = \mu\omega\left(1 + \frac{r_o}{c}\right) \tag{6}$$

Combining Equations 1, 2 and 6, the laminar friction loss over a rotating cylinder is given by:

$$P_f = \omega \int_0^l \int_0^{2\pi} \mu\omega\left(1 + \frac{r_o}{c}\right) r_o\, r_o d\theta dz = 2\pi\mu\omega^2 r_o^2 l\left(1 + \frac{r_o}{c}\right) \tag{7}$$

Also combining Equations 1, 3 and 4 with $r_* = r_o$ and $A = 2\pi r_o l$, the general friction loss over a rotating cylinder is expressed as:

$$P_f = C_f \pi\rho\omega^3 r_o^4 l \tag{8}$$

Further combining Equations 7-8, the laminar skin friction coefficient for a rotating cylinder is obtained:

$$C_f = \frac{2}{Re}\left(1 + \frac{1}{c_r}\right) \tag{9}$$

where Re is the Reynolds number and c_r is the clearance ratio:

$$Re = \frac{\rho\omega r_o^2}{\mu}$$

$$c_r = \frac{c}{r_o}$$

If the clearance ratio is large, the solid surfaces cannot be considered as infinite flat plates and the linear velocity profile assumption is not valid anymore. Instead, a Taylor-Couette velocity profile with no-slip boundary conditions is to be considered [17]:

$$v_\theta(r) = \frac{\omega r_o^2}{(r_o + c)^2 - r_o^2}\left(r - \frac{(r_o + c)^2}{r}\right) \tag{10}$$

Following the same development procedure based on Equation 10, the resulting laminar skin friction coefficient for a rotating cylinder is:

$$C_f = \frac{4}{Re}\frac{(1 + c_r)^2}{(1 + c_r)^2 - 1} \tag{11}$$

As shown in Figure 3, for clearance ratios below 0.02, there is less than 1% difference between Equations 11 and 9. However, for higher clearance ratios, Equation 11 provides significantly higher values of the skin friction coefficient compared to Equation 9 (about 10% higher for a clearance ratio of 0.2).

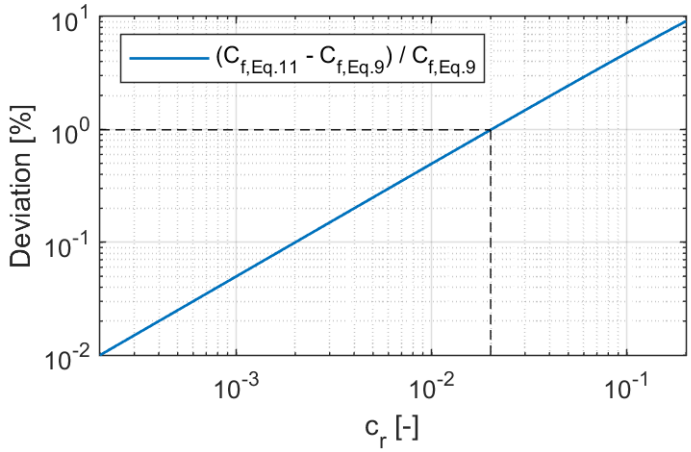

Figure 3: Comparison of the skin friction coefficients obtained using Equation 11 (Taylor-Couette flow) and Equation 9 (Couette flow or linear velocity profile)

2.1.2 Rotating disk

In cylindrical coordinates, the local shear stress throughout the axially extended clearance from an enclosed rotating disk is defined as:

$$\tau_{z\theta} = \mu\left[\frac{1}{r}\frac{\partial v_z}{\partial \theta} + \frac{\partial v_\theta}{\partial z}\right]$$

Considering the situation represented in Figure 2b, and assuming no axial flow and a linear velocity profile (Couette flow) in the tangential direction (Equation 12), the local shear stress acting on the surface of the disk reduces to Equation 13.

$$v_\theta(z) = \frac{\omega r}{c}(z - c) \tag{12}$$

$$\tau_f = \mu\omega\frac{r}{c} \tag{13}$$

Combining Equations 1, 2 and 13, the laminar friction loss over a single-sided rotating disk is given by:

$$P_f = \omega\int_{r_i}^{r_o}\int_0^{2\pi}\mu\omega\frac{r}{c}\,r\,r d\theta dr = \frac{\pi}{2}\mu\omega^2\frac{r_o^4}{c}\left(1 - \frac{r_i^4}{r_o^4}\right) \tag{14}$$

Also combining Equations 1, 3 and 4 with $r_* = r_o$ and $A = \pi\left(r_o^2 - r_i^2\right)$, the general friction loss over a single-sided rotating disk is expressed as:

$$P_f = C_f\frac{\pi}{2}\rho\omega^3 r_o^5\left(1 - \frac{r_i^2}{r_o^2}\right) \tag{15}$$

Further combining Equations 14-15, the laminar skin friction coefficient for a single-sided rotating disk is obtained:

$$C_f = \frac{1 + \lambda^2}{Re\ c_r} \tag{16}$$

where λ is the radius ratio:

$$\lambda = \frac{r_i}{r_o}$$

Alternatively, the friction loss and coefficient can be defined in such a way that the effect of the inner radius is captured in the expression of the skin friction coefficient only:

$$P_f = C_f' \frac{\pi}{2} \rho \omega^3 r_o^5 \tag{17}$$

$$C_f' = \frac{1 - \lambda^4}{Re\ c_r} \tag{18}$$

2.2 State of the art models for non-laminar flow regime

Under non-laminar flow regime, the velocity profile deviates from the linear theory and cannot be expressed in a simple way such as in Equations 5 and 12. The common approach is to apply Equations 8 and 15 (or 17) while providing an empirical expression for the skin friction coefficient that is valid within a certain range of the system's non-dimensional parameters.

2.2.1 Rotating cylinder

The flow surrounding an enclosed rotating cylinder can experience three regimes. At low speed, the steady and purely azimuthal Taylor-Couette flow takes place, leading to the laminar skin friction coefficient from Equation 11 (blue line in Figure 4). Beyond a certain speed threshold, or alternatively a certain Taylor number (Equation 19), the flow remains steady but axisymmetric toroidal vortices start to grow in the annulus [18], which raises the skin friction coefficient [19] (green line in Figure 4). If the clearance ratio is small, the onset of instabilities can be determined from the critical Taylor number presented in Equation 20 [20], which asymptotically tends to a value of 41.1 if the clearance ratio tends to zero (Figure 5). Further increasing the speed, there is a progression of instabilities characterized by wavy vortices, until the flow becomes unsteady. Beyond a Taylor number of 400 [16], the flow is fully turbulent (red line in Figure 4).

$$Ta = \frac{\rho \omega r_o^2}{\mu} \left(\frac{c}{r_o}\right)^{3/2} = Re\ c_r^{3/2} \tag{19}$$

$$Ta_{crit} = \pi^2 \left(\frac{2 + c_r}{2S}\right)^{1/2} \tag{20}$$
$$S = 0.0571(1 - 0.652c_r) + 0.00056(1 - 0.652c_r)^{-1}$$

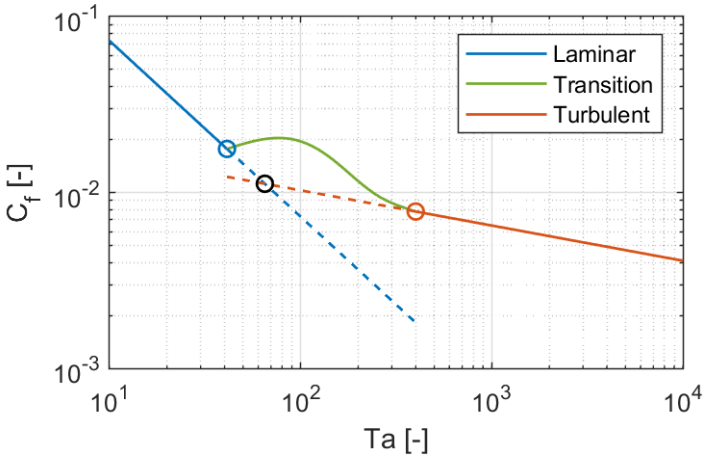

Figure 4: Characteristic evolution of the skin friction coefficient as a function of the Taylor number

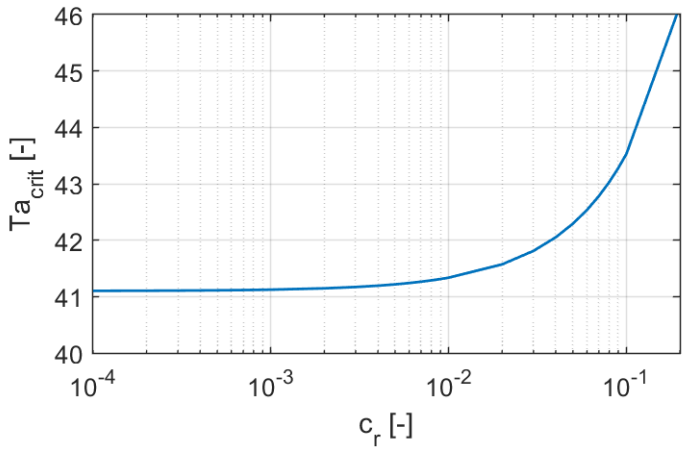

Figure 5: Critical Taylor number characterizing the onset of the formation of Taylor vortices (Equation 20)

Several models [16,21–25] have been proposed to evaluate the skin friction coefficient associated with an enclosed rotating cylinder under non-laminar flow conditions. Multi flow regime models such as the ones by Wendt [21] or Bilgen and Boulos [24] were found to underestimate experimental skin friction coefficients [26]. The model by Mack [16] (Equations 8 and 21) has been applied to estimate windage losses in the air-gap of high-speed electrical machines and showed good agreement with experimental data [13,27] when determining the proportionality coefficient K (Equation 21b) from Mack's laminar skin friction coefficient expression (Equation 21a) evaluated at a critical Taylor number Ta_{crit} = 41.3 (blue and black dots superimposed in Figure 4).

$$C_f = \begin{cases} \dfrac{1.8}{Re\, c_r^{1/4}} \dfrac{(1+c_r)^2}{(1+c_r)^2 - 1}, & Ta < 41.3 \text{ (laminar flow)} \quad (21a) \\ \dfrac{K}{Ta^{1/5}}, & Ta > 400 \text{ (fully turbulent flow)} \quad (21b) \end{cases}$$

The transition regime from laminar to fully turbulent flow (41.1 < Ta < 400) is poorly covered in the literature. Nachouane et al. [19] performed a numerical analysis of the friction loss in this regime. However, the resulting model has not been validated experimentally and there is a large discrepancy with Mack's model in the turbulent flow regime. As a consequence, the state of the art approach is to apply Equation 21b also in the transition regime (red dashed line in Figure 4), which underestimates the actual skin friction coefficient.

2.2.2 Rotating disk

Daily and Nece [28] presented a comprehensive model (Equations 17 and 22) to evaluate the skin friction coefficient associated with an enclosed rotating disk. Their model was validated based on a large set of experiments in which they identified four flow regimes. However, a single radius ratio of 0.1 was investigated, thus making the model inappropriate for disks with a large inner radius. For this reason, the radius ratio λ does not appear in their expression of the skin friction coefficient.

$$C_f' = \begin{cases} \dfrac{1}{Re\ c_r}, & \text{laminar flow, merged boundary layers} \quad (22a) \\ \dfrac{3.7 c_r^{1/10}}{2\pi Re^{1/2}}, & \text{laminar flow, separate boundary layers} \quad (22b) \\ \dfrac{0.08}{2\pi Re^{1/4} c_r^{1/6}}, & \text{turbulent flow, merged boundary layers} \quad (22c) \\ \dfrac{0.102 c_r^{1/10}}{2\pi Re^{1/5}}, & \text{turbulent flow, separate boundary layers} \quad (22d) \end{cases}$$

Daily and Nece provided friction coefficients for various flow patterns (Equation 22) but did not offer corresponding validity ranges. Instead, for a given Reynolds number, all four expressions of the skin friction coefficient need to be evaluated, and the highest value is to be retained.

2.3 Development of new generic models

Since commonly used multi flow regime loss models (Equations 21 and 22) are not consistent with the definition of the skin friction coefficient in the laminar flow regime (Equations 11 and 18), it is proposed to modify them accordingly.

2.3.1 Rotating cylinder

For the skin friction coefficient associated with an enclosed rotating cylinder, the proposed loss model (Equations 8 and 23) is based on Mack's model [16], modified using Equation 11 instead of 21a.

$$C_f = \begin{cases} \dfrac{4}{Re} \dfrac{(1+c_r)^2}{(1+c_r)^2 - 1}, & Ta \le Ta_{crit} \quad (23a) \\ \dfrac{K}{Ta^{1/5}}, & Ta > Ta_{crit} \quad (23b) \end{cases}$$

The proportionality coefficient K (Equation 23b) is determined from the laminar skin friction coefficient expression (Equation 23a) evaluated at a fictitious critical Taylor number (black dot abscissa in Figure 4). This one may be obtained from Equation 20 or may alternatively be a constant than is chosen to best match the experimental data. The transition regime is not captured in this model and the skin friction coefficient is consequently likely to be underestimated for Taylor numbers between 41.1 and 400.

2.3.2 Rotating disk

For the skin friction coefficient associated with an enclosed rotating disk, the proposed loss model (Equations 17 and 24) is based on Daily and Nece's model [28], including, however, the effect of the radius ratio. For each flow regime, the model development procedure is as follows:

- Derive the friction loss expression from Daily and Nece (Equations 17 and 22) with respect to r_o
- Integrate the obtained local friction loss expression from r_i to r_o
- Identify the resulting skin friction coefficient such that it matches the form of Equation 17
- Express the skin friction coefficient as a function of the non-dimensional parameters, which results in the following:

$$C_f' = \begin{cases} \dfrac{1-\lambda^4}{Re\ c_r}, & \text{laminar flow, merged boundary layers} \quad (24a) \\ \dfrac{3.7 c_r^{1/10}\left(1-\lambda^{39/10}\right)}{2\pi Re^{1/2}}, & \text{laminar flow, separate boundary layers} \quad (24b) \\ \dfrac{0.08\left(1-\lambda^{14/3}\right)}{2\pi Re^{1/4} c_r^{1/6}}, & \text{turbulent flow, merged boundary layers} \quad (24c) \\ \dfrac{0.102 c_r^{1/10}\left(1-\lambda^{9/2}\right)}{2\pi Re^{1/5}}, & \text{turbulent flow, separate boundary layers} \quad (24d) \end{cases}$$

As for the original model, all four expressions of Equation 24 have to be evaluated for a given Reynolds number, and the highest value is to be retained.

2.4 Experimental setup and global loss model

2.4.1 The investigated gas bearing supported spindle

The investigated spindle is shown in Figure 6, Figure 7 and Figure 8 and its inertias and dimensions are presented in Table 1. The rotor is composed of a T-shape sleeve, in which a permanent magnet and two balancing plugs are fitted. It is supported on two HGJBs that are rigidly linked together, and a double-sided SGTB. The grooves are machined on the rotating parts for the journal bearings and on the stationary parts for the thrust bearing. The spindle has been designed to operate in air and in halocarbon R245fa beyond 100'000 RPM.

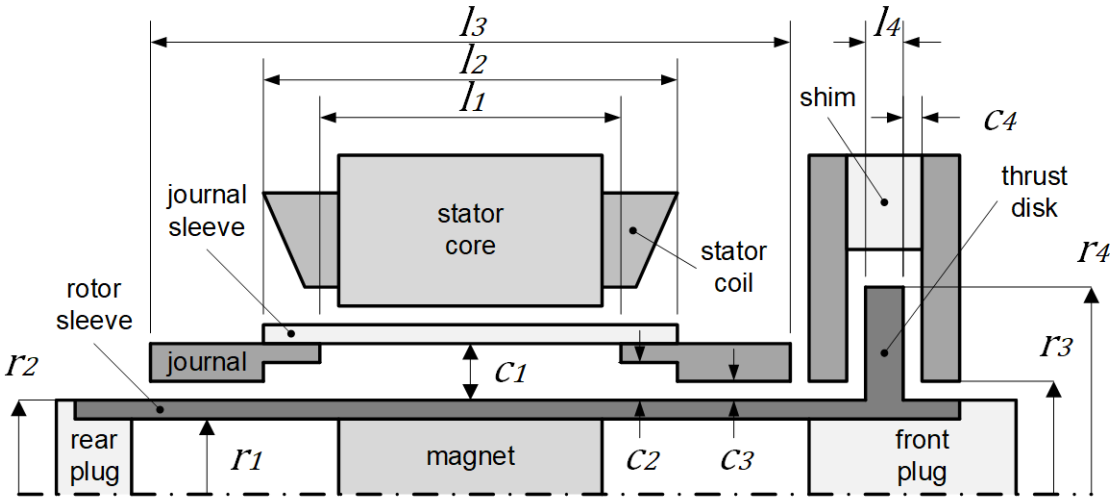

Figure 6: Sketch of the investigated spindle
(see corresponding numerical values in Table 1)

Table 1: Inertias and dimensions of the investigated spindle
(see corresponding symbols in Figure 6)

Parameter	Value
m_s	277.6 g
J_s	20.81±0.1 kg mm^2
l_1	55 mm
l_2	81 mm
l_3	115 mm
l_4	3 mm
r_1	7 mm

Parameter	Value
r_2	8.5 mm
r_3	9 mm
r_4	19.5 mm
c_1	2 mm
c_2	1 mm
c_3	6.5±0.5 µm
c_4	15±0.5 µm

Figure 7: Rotor shaft and bearings

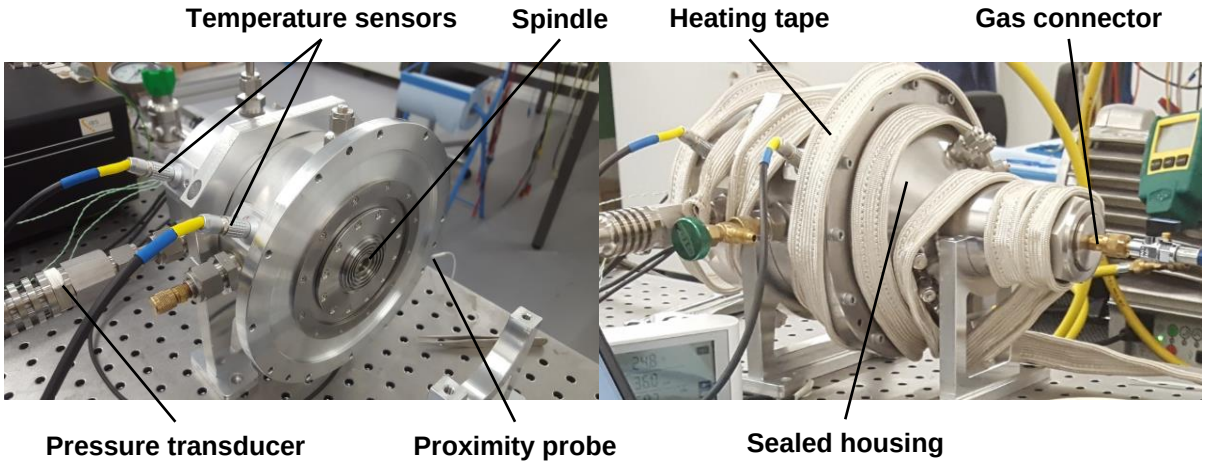

Figure 8: Prototype in open configuration (left) and sealed configuration (right)

The prototype is instrumented with a pressure transducer (± 0.01 bar accuracy), resistance temperature sensors (± 1°C accuracy) glued on the stationary part of the journal bearings, and proximity probes (0.5 nm resolution at 15 kHz bandwidth) measuring the radial displacement of the spindle on both sides of the journal bearings. Since the radial displacements are induced by the unbalance of the spindle, they are harmonic with a period corresponding to the rotational frequency. Therefore, a fast Fourier transform (FFT) of the proximity probe signal allows determining the rotational frequency of the spindle. The sampling rate of the proximity probes is 48 times the nominal rotational frequency in order to ensure a sufficiently high resolution.

2.4.2 Loss measurement procedure

In order to measure the losses, a coast-down test is performed: the spindle is first accelerated beyond nominal speed using a high-frequency drive system, then the power supply is cut and the spindle slows down due to friction. The rate of deceleration is recorded until the spindle stops. To do so, the raw proximity probe data are split into small sets (2^{14} points), on which the FFT is applied to determine the corresponding average rotational frequency. The resulting data are then truncated to remove low-speed points (affected by bearing touchdown) and fitted with respect to time with a 6th order polynomial (Figure 9), which provides a smooth analytical expression for $\omega(t)$. Since there are less points at high speeds due to the higher frictional torque, the fitting operation is weighted such that the highest speed points are also accurately predicted by the polynomial. In order to determine the friction torque T_f, the polynomial is derived once to obtain $d\omega/dt$ and then multiplied by the moment of inertia J_s of the spindle:

$$T_f(t) = -J_s \frac{d\omega}{dt}(t)$$

Finally, the friction power P_f is evaluated as expressed in Equation 1:

$$P_f(t) = T_f(t)\omega(t)$$

The measured friction power is subjected to three sources of error:

- Error on the raw rotational speed obtained from the FFT
- Error on the fitted rotational speed
- Error on the moment of inertia of the spindle

With the considered number of data points per set, the FFT algorithm has a resolution of 293 RPM. However, the fitting operation smoothens this error, which explains why the deviation between the fitted and the raw speed data is very noisy (Figure 9). The consequence is also a negligible error on the rate of change of the speed. Therefore, the error on the friction power δP_f mostly depends on the error on the speed $\delta\omega$ and on the moment of inertia δJ_s:

$$\delta P_f = \frac{\partial P_f}{\partial \omega}\delta\omega + \frac{\partial P_f}{\partial J_s}\delta J_s = -\frac{d\omega}{dt}(J_s\delta\omega + \omega\delta J_s)$$

The error on the speed is defined as the peak deviation between the fitted and the raw speed data from 20 and 100 kRPM. It incorporates the error of the FFT and the error of the fitting operation. The minimum error for the coast-down test in air is ±181 RPM (Figure 9a), while the maximum error for the coast-down test in the high-pressure halocarbon is ±300 RPM (Figure 9b).

The moment of inertia of the spindle (Table 1) was estimated through the 3D CAD drawing of the spindle, for which there is an uncertainty on the density of the involved materials. However, the highest uncertainty results from the balancing procedure. With the mass removed at the tip of the thrust disk and the mass added/removed in the balancing plugs, the moment of inertia may deviate by ± 0.1 kg mm^2.

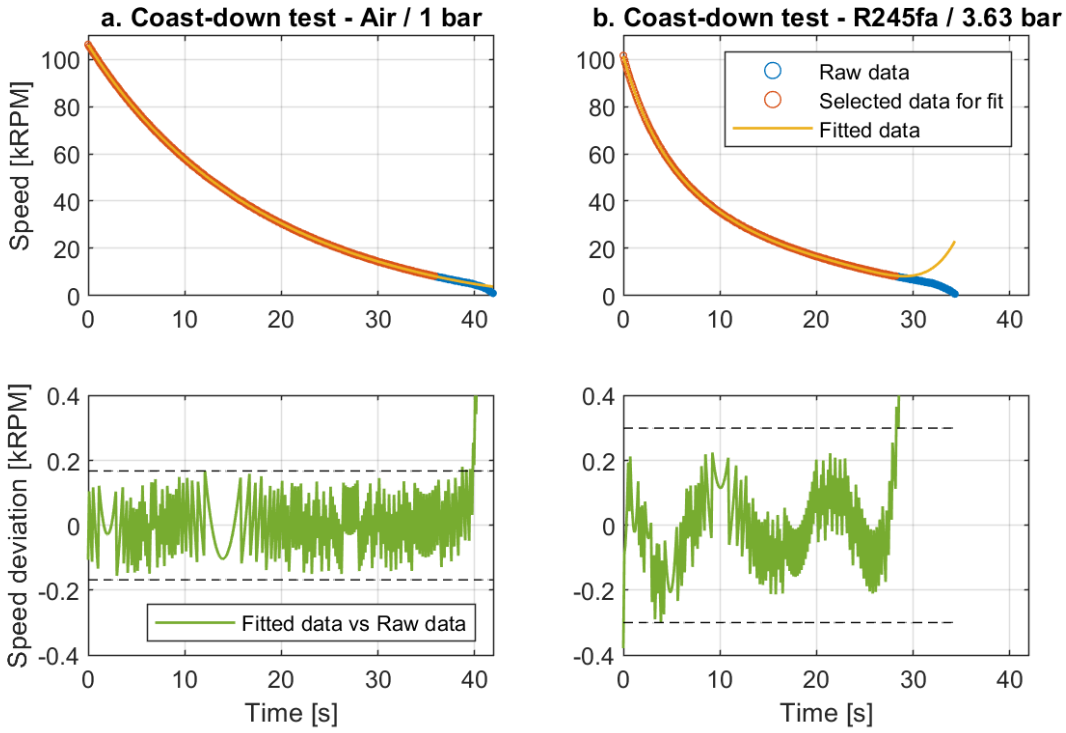

Figure 9: Data post-processing examples
(a) Most accurate fit in ambient air / (b) Least accurate fit in high-pressure halocarbon

2.4.3 Loss components and loss models combination

The spindle is exposed to four main source of losses (Equation 25):

- Windage loss in the two HGJBs
- Windage loss in the double-sided SGTB
- Windage loss in the air-gap of the electrical machine
- Iron loss in the stator of the electrical machine, induced by the rotating magnetic field of the permanent magnet

$$P_f = P_{HGJB} + P_{SGTB} + P_{gap} + P_{iron} \tag{25}$$

Grooved bearing losses are normally computed by assuming Couette flow in the narrow bearing clearance (Equations 7 and 14). However, HGJB losses tend to be lower compared to an equivalent plain bearing [7]. In order to improve the loss prediction, Schiffmann [8] proposed to divide the bearing surface into a region of nominal clearance and a region of higher clearance (nominal clearance + groove depth), for which the friction loss is therefore reduced. With this approach, the model assumes a "perfect" flow regime transition at each groove edge. This assumption is usually made in grooved bearing models evaluating the pressure field in the bearing clearance, through the Reynolds equation and the narrow groove theory [29]. The same approach is pursued here, based however, on generalized expressions of the friction loss (Equations 8 and 17) instead of laminar ones. Hence, the losses of the two journal and of the double-acting thrust bearings (Equations 26 and 27) are subdivided into three components, corresponding to each part of the bearing surface (Figure 10 and Figure 11):

- Loss over the grooved fraction of the grooved surface
- Loss over the ungrooved fraction of the grooved surface
- Loss over the smooth surface

$$P_{HGJB} = 2\left[C_f\left(\frac{\rho\omega r_o^2}{\mu}, \frac{c+h_g}{r_o}\right)\pi\rho\omega^3 r_o^4 l\alpha\gamma + C_f\left(\frac{\rho\omega r_o^2}{\mu}, \frac{c}{r_o}\right)\pi\rho\omega^3 r_o^4 l(1-\alpha\gamma)\right] \quad (26)$$

$$P_{SGTB} = 2\left[C_f'\left(\frac{\rho\omega r_o^2}{\mu}, \frac{c+h_g}{r_o}, \frac{r_s}{r_o}\right)\frac{\pi}{2}\rho\omega^3 r_o^5\alpha + C_f'\left(\frac{\rho\omega r_o^2}{\mu}, \frac{c}{r_o}, \frac{r_s}{r_o}\right)\frac{\pi}{2}\rho\omega^3 r_o^5(1-\alpha) + C_f'\left(\frac{\rho\omega r_s^2}{\mu}, \frac{c}{r_s}, \frac{r_i}{r_s}\right)\frac{\pi}{2}\rho\omega^3 r_s^5\right] \quad (27)$$

where the groove width ratio α, and the groove length ratio γ are defined as:

$$\alpha = \frac{w_g}{w_g + w_r}, \qquad \gamma_{HGJB} = \frac{l - l_s}{l}, \qquad \gamma_{SGTB} = \frac{r_o - r_s}{r_o - r_i}$$

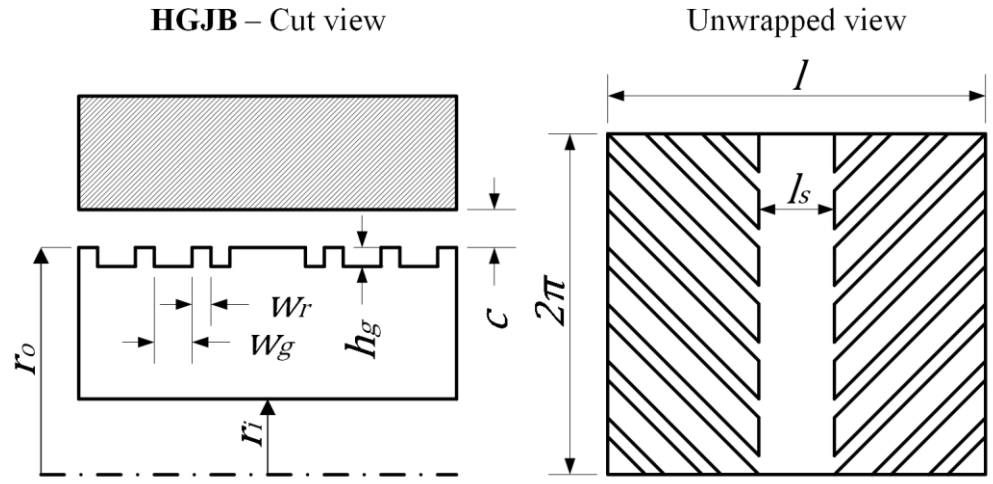

Figure 10: Sketch of a herringbone-grooved journal bearing (arbitrary number of grooves)

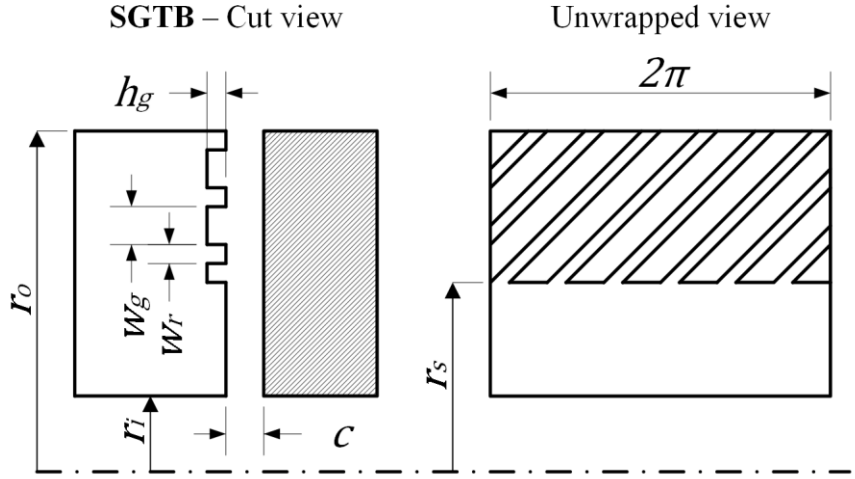

Figure 11: Sketch of a pump-in spiral-grooved thrust bearing (arbitrary number of grooves)

The design parameters of the investigated bearings are presented in Table 2. In view of the high rotational speeds and very narrow gas bearing clearances, the journal bearing clearance is corrected with the effect of the centrifugal growth of the rotor (Equation 28 [30]). Since the rotating and stationary parts of the journal bearings are made of the same material, the thermal growth is assumed not to affect the clearance. Furthermore, due to a load capacity much higher than the rotor weight and an operation beyond the cylindrical and conical modes of the rotor-bearing system, the static and dynamic

eccentricities of the rotor in the journal bearings are very low at high speed (confirmed by the proximity probe measurements). Similarly, due to the absence of axial load (no turbine rotor), the thrust disk is assumed to be centered in the thrust bearing, thus justifying Equation 27.

Table 2: Dimensions of the investigated bearings

Parameter	HGJB	SGTB
l	$(l_3 - l_2)/2$	-
r_o	r_2	r_4
r_i	r_1	r_3
c	Equation 28	c_4
h_g	13 µm	9 µm
α	0.65	0.4
γ	1	0.4333

$$c = c_3 - \left(\frac{3+\nu_s}{4} r_i^2 + \frac{1-\nu_s}{4} r_o^2\right)\frac{\rho_s}{E_s}\omega^2 r_o \tag{28}$$

In Equation 28, c_3 is the journal bearing clearance at zero speed, while ρ_s, E_s and ν_s are the density, Young's modulus and Poisson's ratio of the spindle material (Table 3), respectively.

Table 3: Spindle material properties

Parameter	Value
ρ_s	14550 kg/m^3
E_s	605 GPa
ν_s	0.24
β_s	5.1 µm/m-K

The windage loss in the air-gap of the electrical machine (Equation 29) is subdivided into two components according to the spindle layout (Figure 6) and based on the generalized friction loss expression for enclosed rotating cylinders (Equation 8):

$$P_{gap} = C_f\left(\frac{\rho\omega r_2^2}{\mu}, \frac{c_1}{r_2}\right)\pi\rho\omega^3 r_2^4 l_1 + C_f\left(\frac{\rho\omega r_2^2}{\mu}, \frac{c_2}{r_2}\right)\pi\rho\omega^3 r_2^4 (l_2 - l_1) \tag{29}$$

The needed thermophysical properties of the fluids, i.e. the density and dynamic viscosity, are calculated using a commercial database [31]. The uncertainties on the density and viscosity of R245fa are 0.3% and 2% respectively, in the gas phase.

Finally, the iron loss has been estimated at various rotor speeds by performing finite element (FE) based electromagnetic simulations of the electrical machine without load. The resulting data (Figure 12) has been fitted with a 3rd order polynomial (Equation 30) with a maximum relative error of 0.6% at 30 kRPM. Below this speed, no simulations were performed and the iron loss model is likely to poorly predict the actual loss.

$$P_{iron} = 8.078 \cdot 10^{-4}\omega + 2.929 \cdot 10^{-7}\omega^2 + 6.052 \cdot 10^{-12}\omega^3 \tag{30}$$

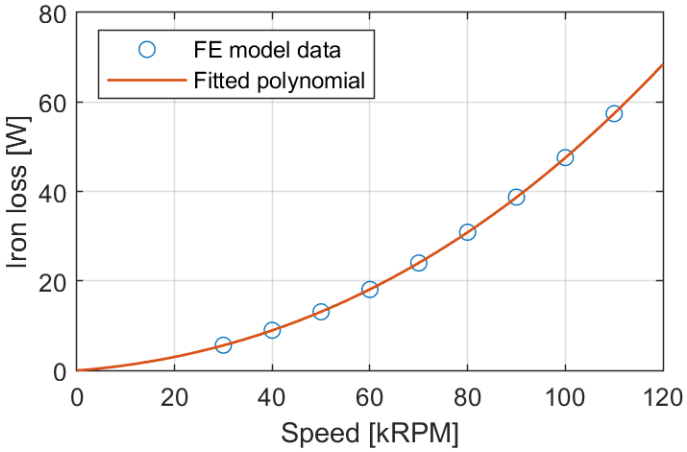

Figure 12: Iron loss simulated data and fit

In order to compare the predicted and measured friction loss of the spindle at a given speed, the relative loss deviation defined by Equation 31 is used.

$$\varepsilon = \frac{P_{f,predicted}(\omega) - P_{f,measured}(\omega)}{P_{f,measured}(\omega)} \tag{31}$$

3. Results and discussion

3.1 Measurements

Coast-down tests were conducted first in ambient air and then in halocarbon R245fa at various pressures ranging from 1.4 to 3.6 bar. Coast-down tests in air were performed several times (Figure 13) in order to ensure the repeatability of the measurement method. At nominal speed (100 kRPM), the relative difference between the three measurements is smaller than 0.3%. Figure 14 presents the measured losses in air and in R245fa at three different pressure levels, together with the corresponding error bars. At nominal speed, the losses reach 140±0.9 W in air, while rising up to 325±2.5 W in the organic fluid. The increase in pressure substantially increases the losses. Since the iron losses are independent of pressure and the fluid viscosity is not significantly affected by pressure, this means that the change in losses with pressure can be attributed to the change in fluid density. However, under laminar flow, the friction losses are independent of density (Equations 7 and 14). Hence, the loss increase with pressure relates to non-laminar flow patterns, most likely in the large clearance of the electrical machine, but also in the narrow gas bearing clearances.

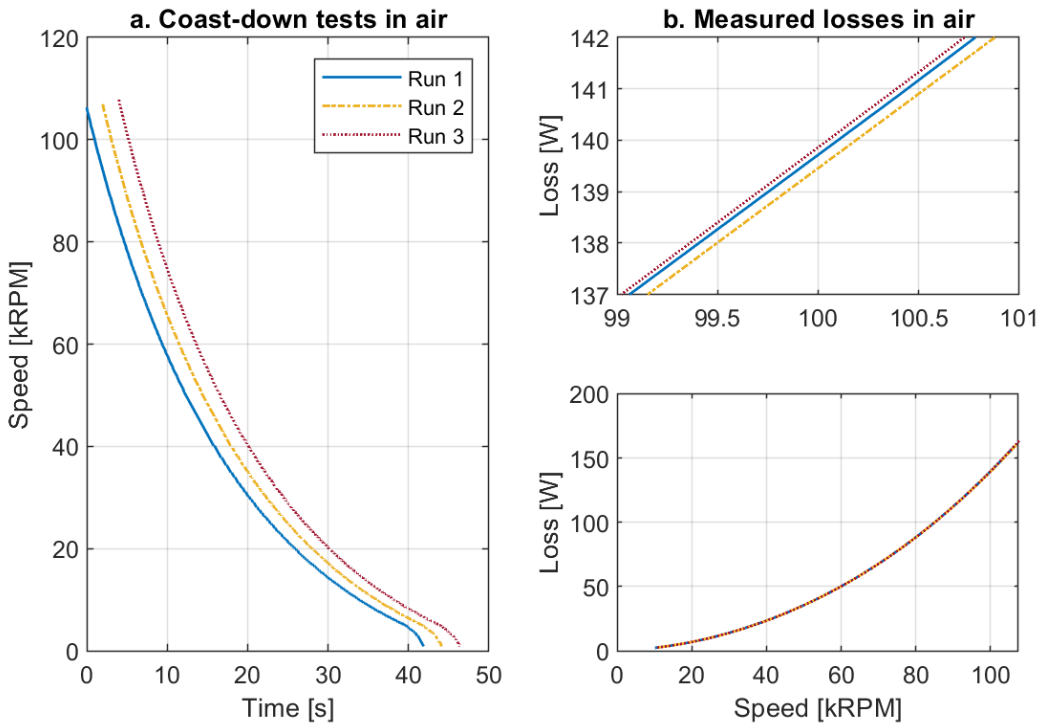

Figure 13: Coast-down measurement method repeatability

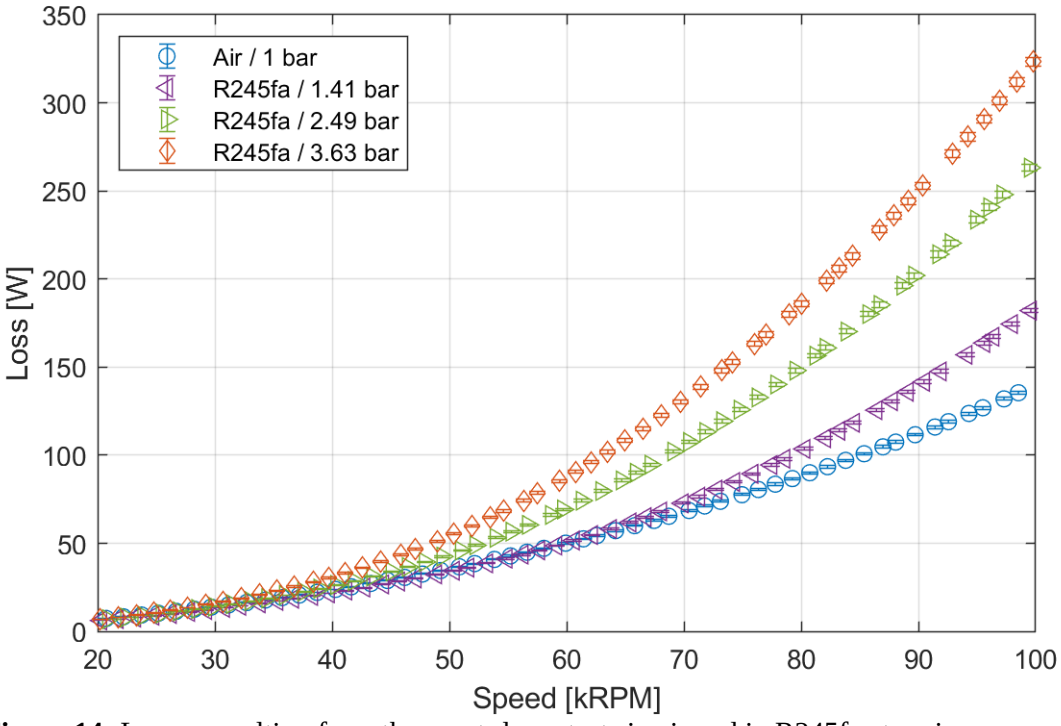

Figure 14: Losses resulting from the coast-down tests in air and in R245fa at various pressures

3.2 Data and models comparison

3.2.1 Reference (state of the art) model

The proposed approach to evaluate the baseline loss of the spindle (Equations 25-30) is to apply the state of the art skin friction coefficients based on Couette flow (Equations 9 and 18) in the narrow gas

bearing clearances and from Mack (Equation 21) in the air-gap. Figure 15 presents the relative deviation (Equation 31) between the prediction of this reference model and the experimental loss as a function of the rotational speed. At low speed (< 25 kRPM), the experimental loss is always underestimated by the model, but the deviation is small (< 10%). At nominal speed (100 kRPM), the model overestimates the measured loss by up to 5% in air, while in R245fa, the model underestimates the measured loss by up to 36% at the highest pressure. The distribution of the losses shown in Figure 16 suggests that at high speed, the air-gap loss component is nearly negligible in air, while it is dominant for the organic fluid test cases, especially at high pressure. Hence, the air-gap turbulence seems to be captured by Mack's model, yet is not sufficient to explain the significant deviation with the experimental data.

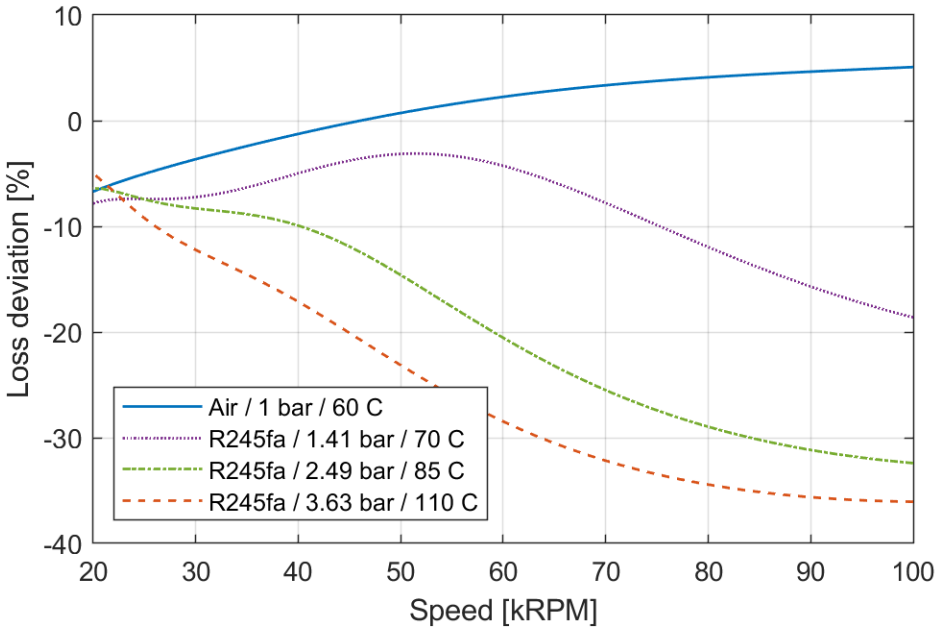

Figure 15: Deviation of the reference loss model with respect to the experimental loss

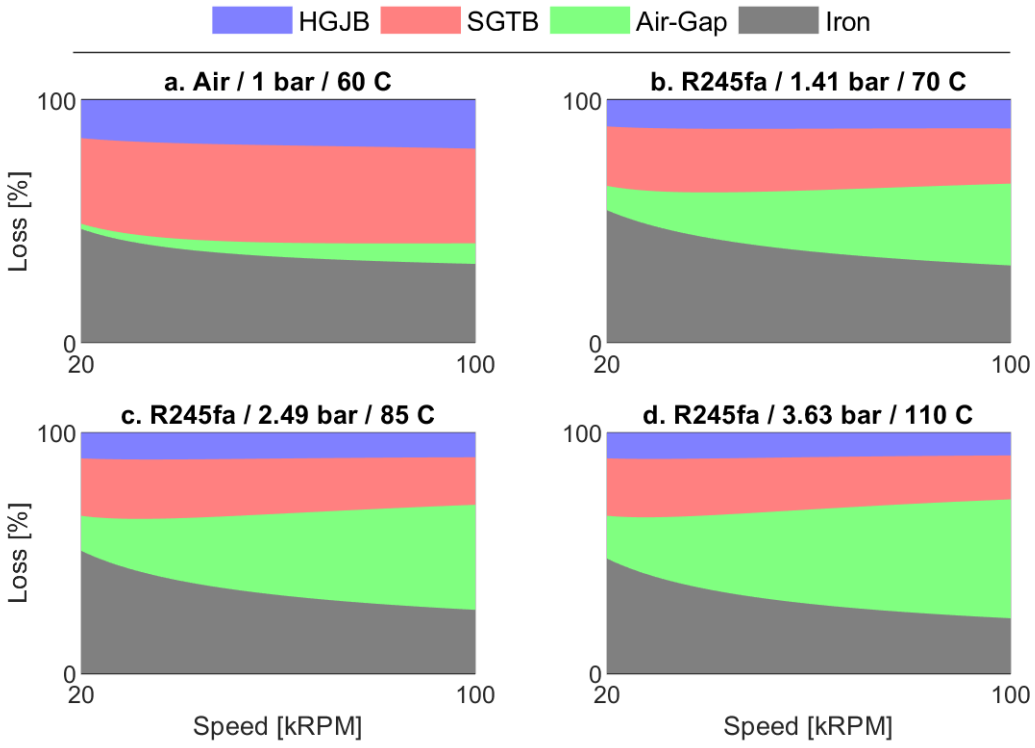

Figure 16: Loss distribution based on the reference loss model

3.2.2 Model with turbulence in the thrust bearing

In order to assess the potential effect of turbulence in the thrust bearing, its loss (Equation 27) is computed using the generic skin friction coefficient expression proposed by the authors for enclosed rotating disks (Equation 24). The journal bearings and air-gap losses are still computed using Equations 9 and 21, respectively. Figure 17 presents the resulting relative deviation between the prediction of this model and the experimental data. In air, the deviation remains identical to the one obtained with the reference model due to the absence of a transition in the flow regime (Figure 18a). However, the deviation is considerably reduced (max 6.8%) in the organic fluid due to a transition to the laminar flow regime with separate boundary layers (Figure 18bcd). The transition occurs in all regions of the thrust bearing, but mostly in the grooves. The transition speeds are also lower at higher pressures, which is in agreement with the theory.

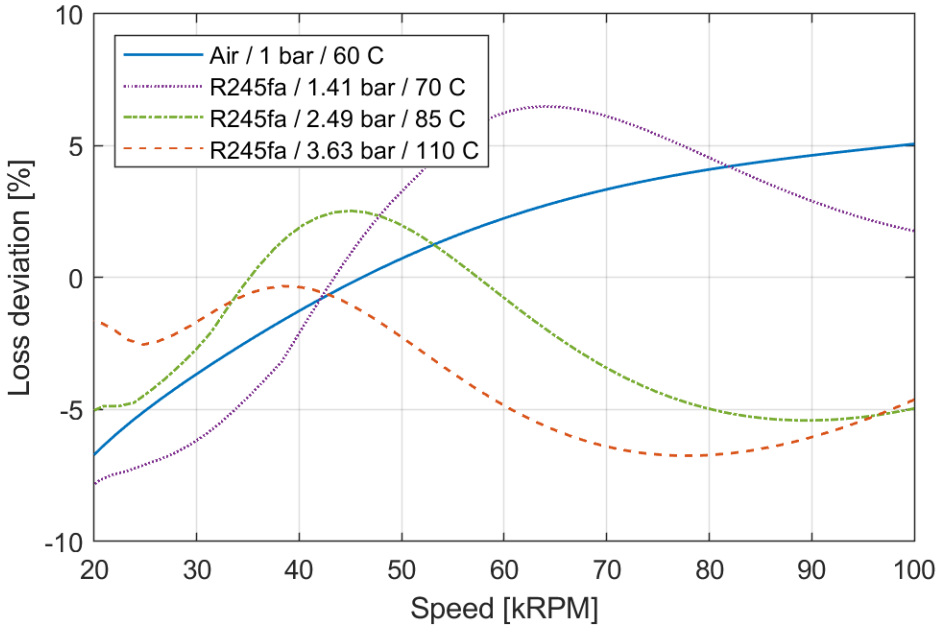

Figure 17: Deviation of the loss model accounting for turbulence in the thrust bearing

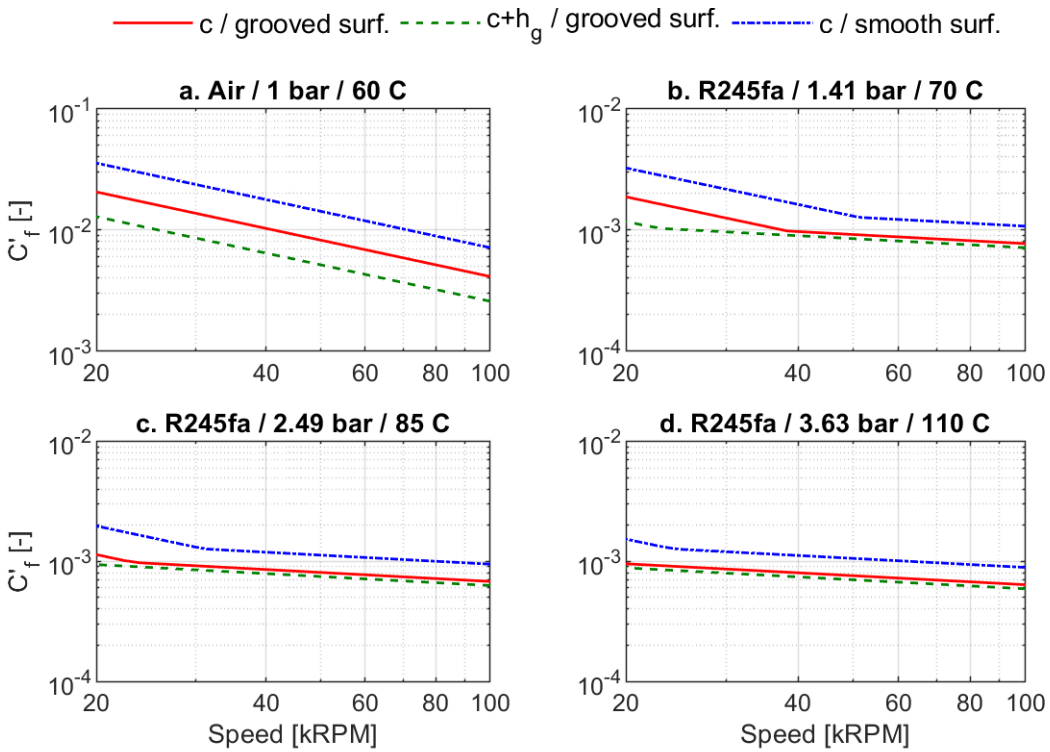

Figure 18: Skin friction coefficients in the SGTB using Equation 24

3.2.3 Model with turbulence in both the journal and thrust bearings

In the previous subsections, the losses of the journal bearings and the air-gap are computed using distinct expressions of the skin friction coefficient, although they are both essentially enclosed rotating cylinders. According to the flow similarity principles, it should be possible to treat them in an identical manner, provided that the treatment is non-dimensional. Therefore, the journal bearings and air-gap losses are computed using the generic skin friction coefficient expression proposed by the authors for enclosed rotating cylinders (Equation 23). The thrust bearing loss is still computed using Equation 24, which accounts for multiple flow regimes. Figure 19 presents the resulting relative deviation between the prediction of this model and the experimental data. Equation 23 is first applied with a fixed critical Taylor number of 41.3, as suggested in Mack's model. The resulting predictions overestimate the experimental data for all test cases, by up to 9% in air and 18% in R245fa. The second attempt, using Equation 20 as the critical Taylor number slightly improves the match with the experimental data, with overestimations up to 8% in air and 15% in R245fa. The third attempt consisted in identifying the critical Taylor number that best match the experimental data in the investigated speed range and considering the four test cases. The resulting optimal value was Ta_{crit} = 67. In air, the new model prediction is identical to the reference model prediction and the maximum relative deviation is 5% at high speed (Figure 19a). In the organic fluid, the model mostly overpredicts the low-pressure data (Figure 19b), while it mostly underpredicts the higher-pressure data (Figure 19cd), with a peak deviation of 6.5%.

The new model match with the experimental data is slightly improved compared to the model accounting for turbulence in the thrust bearing only. This is due to the transition to the turbulent flow regime in the grooves of the journal bearings at high speed and high pressure (Figure 20cd). In air and in the low-pressure organic fluid, the flow regime is suggested to remain laminar (Figure 20ab). With the new model, the thrust bearing loss is suggested to become dominant at high speed for all test cases (Figure 21). This is an important aspect to consider in the thermal management of the spindle. Finally, the proposed loss model predicts the measured friction loss of the spindle operated both in air and in a dense gas with a much better accuracy compared to the state of the art model (Figure 22 vs Figure 1).

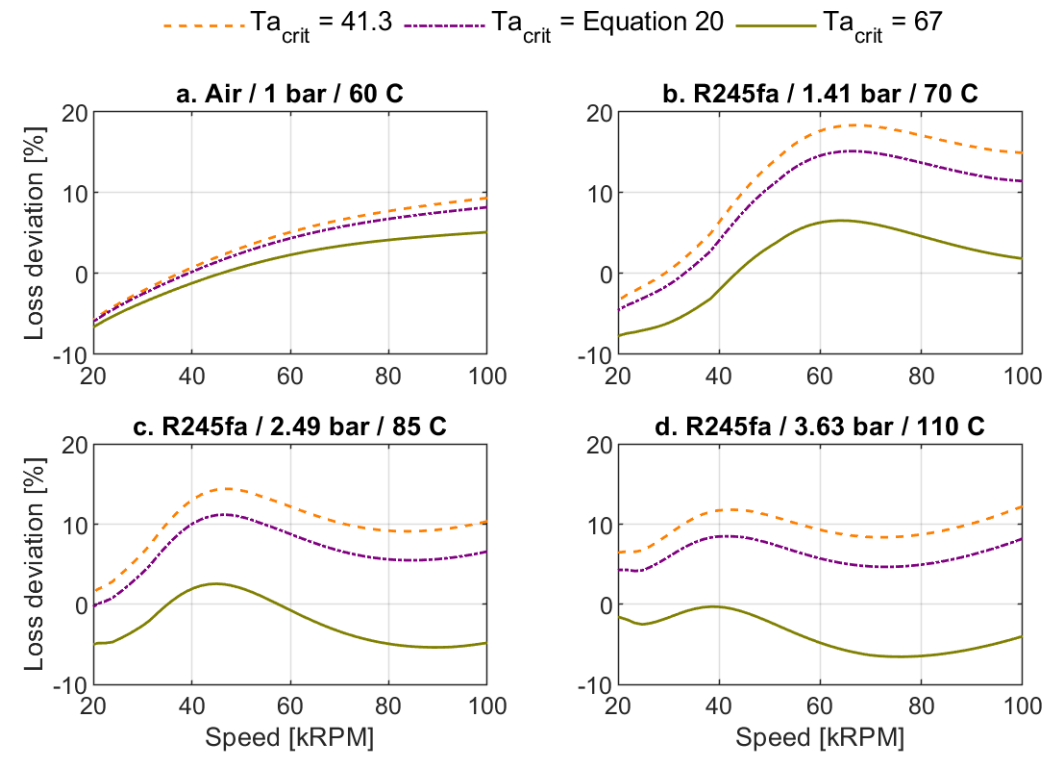

Figure 19: Deviation of the loss model accounting for turbulence in the journal and thrust bearings, and using the same skin friction coefficient expression (Equation 23) to predict the journal bearings and the air-gap losses

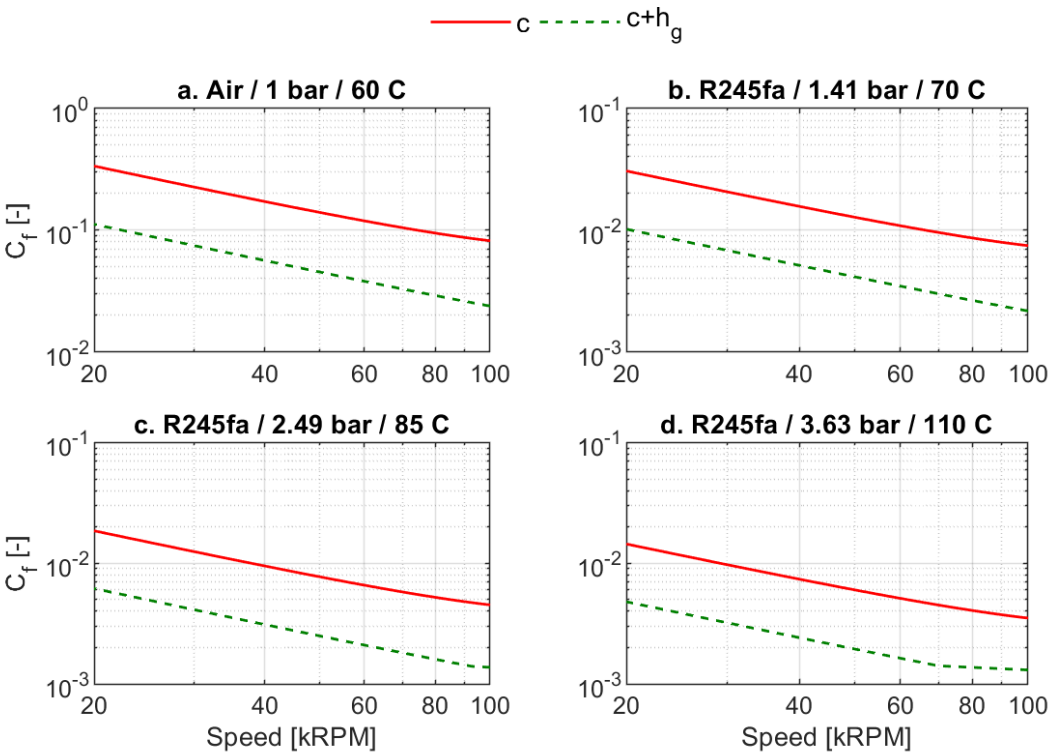

Figure 20: Skin friction coefficients in the HGJB using Equation 23 with Ta_{crit} = 67

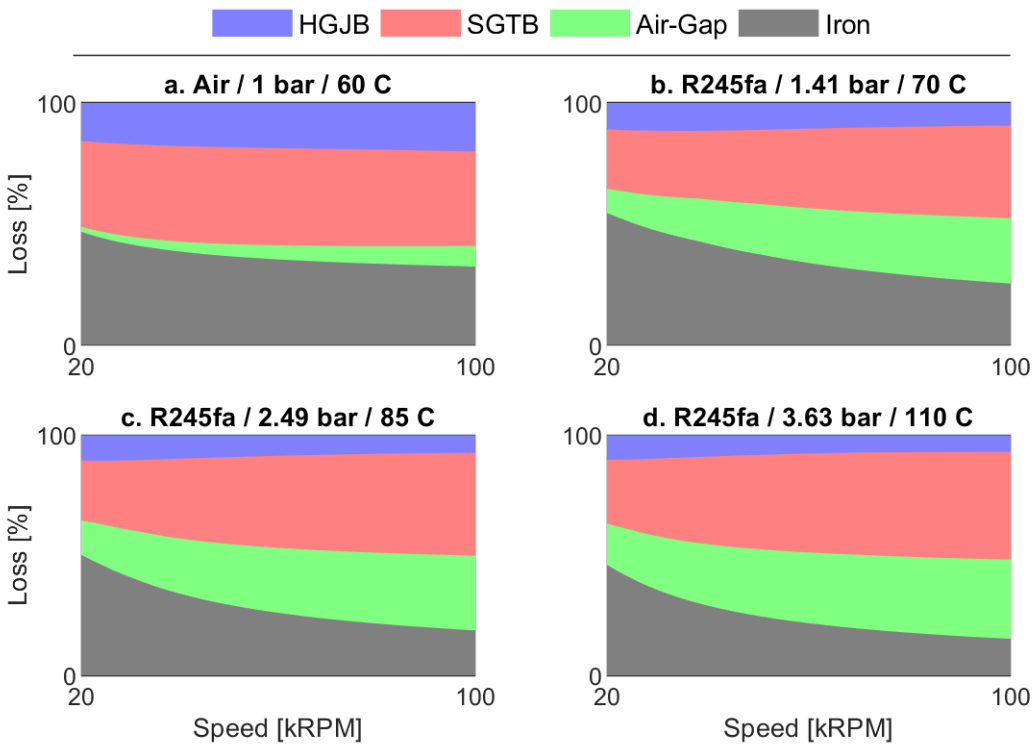

Figure 21: Loss distribution based on the new loss model with Ta_{crit} = 67

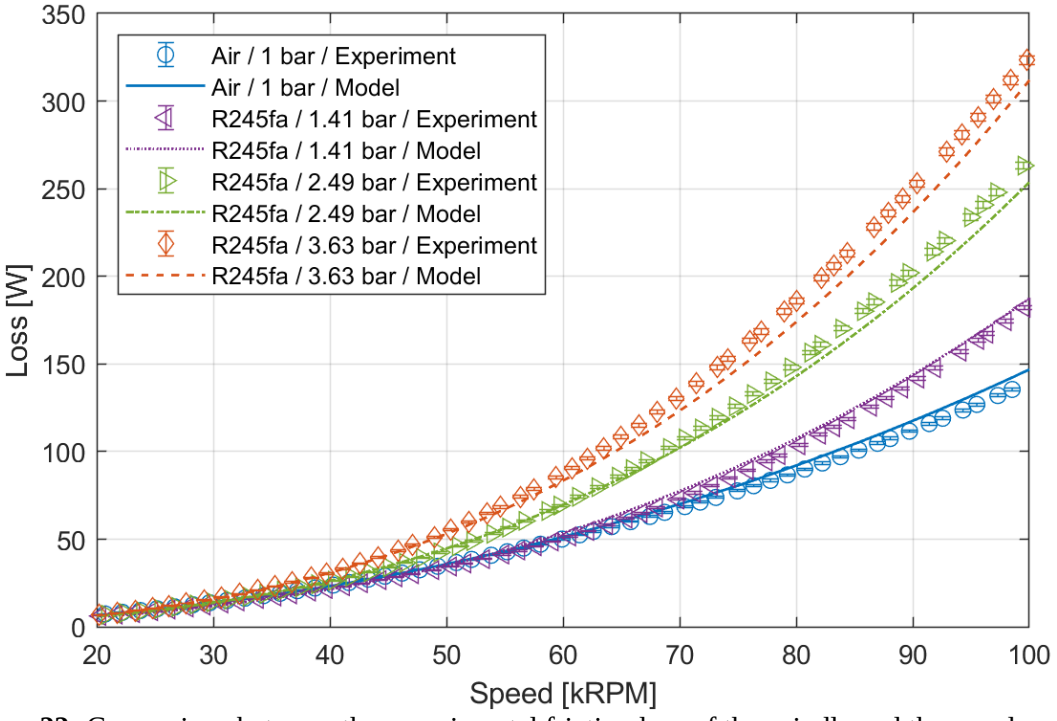

Figure 22: Comparison between the experimental friction loss of the spindle and the new loss model with Ta_{crit} = 67

3.3 Sensitivity analysis

As shown in section 2.4.3, windage losses are affected by rotational speed, geometry and fluid properties. While the rotational speed and most of the dimensions are measured with a high degree of confidence, the narrow gas bearing clearances are subjected to an uncertainty of ± 0.5 µm. In addition,

fluid density and viscosity are dependent on pressure and temperature, which are also measured with uncertainty. For the evaluation of the loss model, the used nominal pressure and temperature are the ones measured when the spindle starts decelerating, although both are slightly dropping during the deceleration. Moreover, the temperature is measured on the outer part of the two journal bearings and then averaged, but a significant temperature shift is observed between the front and the rear journal (up to 6.3 K in the high-pressure R245fa). Finally, since losses are generated within the clearances, the fluid temperature is expected to be higher than the measured temperature, especially in the thrust bearing and the air-gap, where a large fraction of the losses is suggested to be generated, according to the new model. Hence, the uncertainties are estimated as ± 0.02 bar for the pressure and ± 10°C for the temperature. A subsequent uncertainty is linked to the relative thermal growth of the thrust disk compared to the shim of the thrust bearing (Figure 6). A worst case scenario would be that the shim remains at ambient temperature T_{amb} (20°C) while the thrust disk is heated up due to the losses in the fluid film. Since no temperature measurements of the thrust bearing are available, the SGTB clearance reduction is estimated based on the average temperature T measured on the journals:

$$\delta c_{SGTB} = -\frac{\beta_s l_4 (T - T_{amb})}{2}$$

With this approach, the SGTB clearance may be reduced by 0.3 µm in the ambient air and by 0.7 µm in the high-pressure R245fa. Figure 23 presents the relative deviation between the prediction of the new loss model (with Ta_{crit} = 67) and the experimental data, taking into account the uncertainties on temperature, pressure and clearance. Note that the uncertainties on the density and viscosity of the fluid (calculated based on pressure and temperature) are neglected. The highest deviation (+10.3%) is observed in air at high speed. The main cause is the reduction of the SGTB clearance due to the superimposed effects of the manufacturing and thermal growth uncertainties. Temperature and HGJB clearance uncertainties also have a significant effect on the loss prediction. While an increase in bearing clearance induces a reduction in bearing loss, an increase in temperature increases the fluid viscosity and consequently the bearing loss, due to the laminar flow regime. In the organic fluid, however, the deviation is smaller and the effect of temperature is dominant and reversed. Indeed, an increase in temperature increases viscosity but also decreases density, which in turns reduces the air-gap and SGTB losses due to the non-laminar flow regime. In conclusions, taking into account the uncertainties, the new model predicts the experimental loss of the spindle within ± 10% (Figure 23).

While the uncertainty on pressure does not significantly change the predicted losses, a further aspect that could affect the windage losses is the pressurization of the fluid within the grooved bearings. Indeed, in case of non-laminar flow, an increase in pressure and consequently in density is expected to raise the losses. In order to assess this effect, the losses are calculated based on the average pressure between the boundary and peak pressures within the bearing clearance. The peak pressure is calculated following the methodology presented by Schiffmann [8] for both the journal and the thrust bearing. The results are presented in Figure 24. In air, there is no loss increase since the bearings always experience laminar flow. In R245fa however, the losses tend to increase, especially at high speed. In the low-pressure case (Figure 24b), for which the model overestimates the data, this causes the relative deviation to increase up to 7% due to the thrust bearing only. However, in the high-pressure cases (Figure 24cd), for which the model underestimates the data, the relative deviation is reduced to 6% due to both the thrust and journal bearings. Indeed, the onset of turbulence in the journal bearings occurs at lower speed due to the increase in pressure and density of the fluid. Hence, if the effect of pressurization is considered in the journal bearings only, the relative deviation remains unchanged at low pressure and is reduced at high pressure. It is also likely that the average pressure assumption is not applicable to the thrust bearing. Nevertheless, the effect of pressurization in the gas bearings turns out to be minor compared to the effect of the uncertainty on the clearance and the temperature.

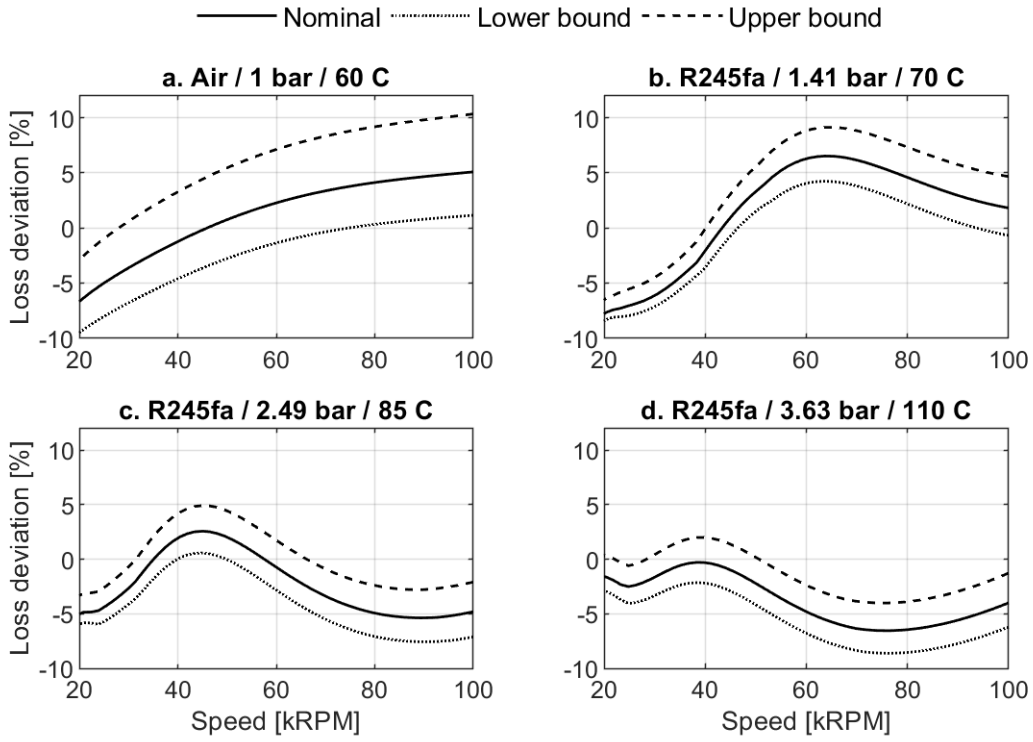

Figure 23: Deviation of the new loss model with Ta_{crit} = 67,
accounting for uncertainty on temperature (± 10°C), pressure (± 0.02 bar), bearing clearances due to manufacturing (± 0.5 µm), and SGTB clearance due to thermal growth of the thrust disk

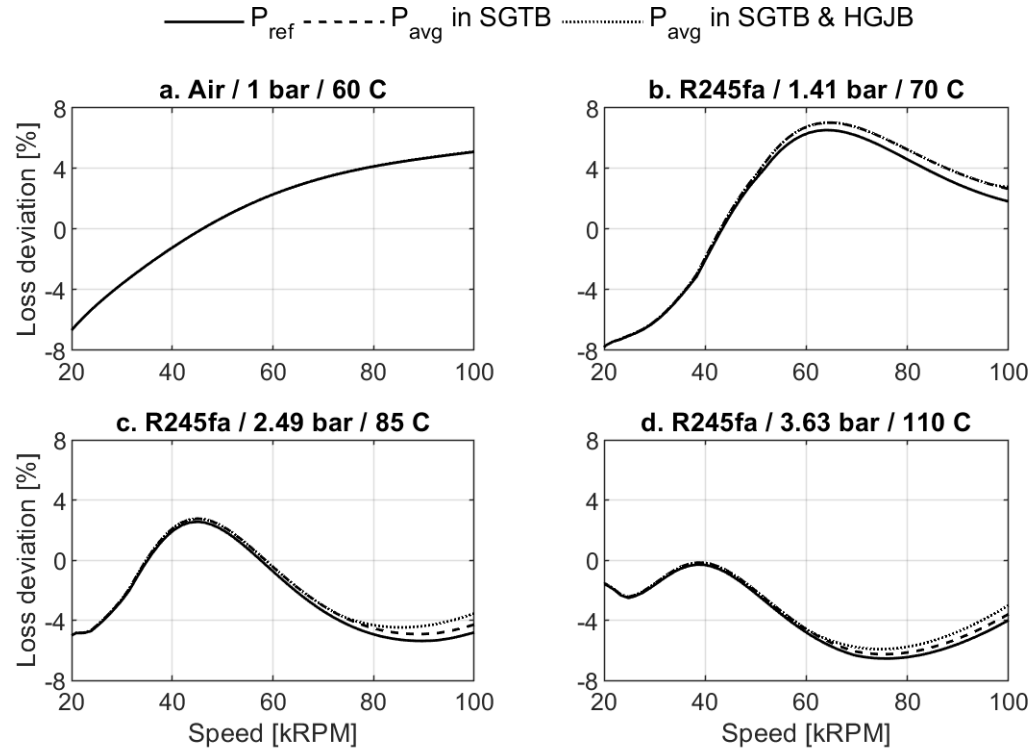

Figure 24: Deviation of the new loss model with Ta_{crit} = 67,
accounting for the effect of pressurization in the gas bearings

4. Conclusions and outlook

In this paper, generic models are proposed to evaluate the skin friction coefficient acting on enclosed rotating disks and cylinders under various flow regimes, typical of gas-lubricated journal/thrust bearings and electrical machine air-gaps. In particular, a model taking into account the inner radius of the disk is developed. The models are compared with experimental data obtained from coast-down tests of a high-speed spindle supported on gas bearings, operated in air and in halocarbon R245fa at various pressures. The measured loss is a combination of windage losses in (1) the two herringbone-grooved journal bearings, (2) the double-sided spiral-grooved thrust bearing, (3) the air-gap of the electrical machine, and of (4) the iron loss in the stator of the electrical machine.

The iron loss is estimated through finite element based electromagnetic simulations of the electrical machine at various speeds and then by fitting the resulting data with a polynomial. The windage losses are first computed considering state of the art laminar flow loss models in the gas bearings and an experimentally validated laminar-turbulent flow loss model in the air-gap. This reference approach predicts the air data with a good accuracy (deviation less than 5%) but underestimates the organic fluid data by up to 36%. This deviation is considerably reduced (max 6.8%) when applying the proposed multi flow regime loss model for enclosed rotating disks to the thrust bearing. Finally, the proposed laminar-turbulent flow loss model for enclosed rotating cylinders is simultaneously applied to the journal bearings and the air-gap. A peak deviation of 6.5% is maintained among all test cases (air and organic fluid at various pressures) when setting the critical Taylor number to 67 instead of the theoretical value characterizing the onset of growth of Taylor vortices. This artificial shift in the critical Taylor number can be associated to the fact that the model does not capture the phenomena in the transition flow regime.

Taking into account the uncertainties on the bearing clearances, as well as on the operating pressure and temperature, a ±10% agreement with the experimental data is obtained. Finally, taking into account the pressurization of the fluid in the gas bearings, the onset of turbulence occurs at lower speed and the predicted loss increases in the organic fluid. If the pressurization is considered in the journal bearings only, the resulting deviation between the model and the experimental data is reduced. However, accounting for the pressurization in the thrust bearing may increase the deviation, possibly due to the average pressure assumption made in the calculation.

While the proposed loss model predicts the measured friction loss of the spindle operated both in air and in a dense gas with a much better accuracy compared to the state of the art model, uncertainty remains with regards to the iron loss model and the actual distribution of losses. Furthermore, the experimental investigation was conducted with a fixed spindle design, and therefore, no sensitivity analysis was performed on the air-gap clearance, the bearing clearances or the bearing groove geometries. The individual loss models (journal, thrust, air-gap, iron) will consequently require further validation.

Nomenclature

Symbols

A	Area	m^2
$C_f^{(\prime)}$	Skin friction coefficient	$-$
c	Clearance	m
c_r	Clearance ratio	$-$
E	Young's modulus	Pa
h	Depth	m
J	Moment of inertia	$kg \cdot m^2$
K	Coefficient	$-$
l	Axial length	m
P	Power loss	W
p	Pressure	Pa
Re	Reynolds number	$-$
r	Radius, Radial coordinate	m
T	Temperature	K
T	Torque	$N \cdot m$
Ta	Taylor number	$-$
t	Time	s
v	Velocity	m/s
w	Width	m
z	Axial coordinate	m
α	Groove width ratio	$-$
β	Thermal expansion coefficient	$1/K$

γ	Groove length ratio	$-$
δ	Deviation	
ε	Relative loss deviation	$-$
θ	Tangential coordinate	rad
λ	Radius ratio	$-$
μ	Dynamic viscosity	$Pa \cdot s$
ν	Poisson's ratio	$-$
ρ	Density	kg/m^3
τ	Shear stress	Pa
ω	Angular speed	rad/s

Subscripts

1	see Figure 6
2	see Figure 6
3	see Figure 6
4	see Figure 6
f	Friction
g	Groove
i	Inner
o	Outer
r	Ridge, Radial coordinate
s	Spindle, Smooth surface
z	Axial coordinate
θ	Tangential coordinate

Acronyms

CAD	Computer-aided design
FE	Finite element
FFT	Fast Fourier transform
HGJB	Herringbone-grooved journal bearing
RPM	Revolutions per minute
SGTB	Spiral-grooved thrust bearing

Acknowledgement

The development of the experimental setup presented in this work was supported by Moving Magnet Technologies (MMT) SA. In particular, the design and finite element based simulations of the permanent-magnet machine were conducted by Mr. Stéphane Tavernier. The authors also thank their colleague Mr. Eliott Guenat for his fruitful suggestions and review of the paper.

References

[1] Celeroton AG, "Launch of Turbo Compressors with Gas Bearings" [Online]. Available: https://www.celeroton.com/en/about-us/news/detail/launch-of-turbo-compressors-with-gas-bearings.html. [Accessed: 03-Mar-2020].

[2] Wagner, P. H., Van herle, J., and Schiffmann, J., 2020, "Theoretical and Experimental Investigation of a Small-Scale, High-Speed, and Oil-Free Radial Anode Off-Gas Recirculation Fan for Solid Oxide Fuel Cell Systems," J. Eng. Gas Turbines Power, **142**(4).

[3] Wagner, P. H., Wuillemin, Z., Constantin, D., Diethelm, S., Van herle, J., and Schiffmann, J., 2020, "Experimental Characterization of a Solid Oxide Fuel Cell Coupled to a Steam-Driven Micro Anode off-Gas Recirculation Fan," Applied Energy, **262**, p. 114219.

[4] Schiffmann, J., and Favrat, D., 2009, "Experimental Investigation of a Direct Driven Radial Compressor for Domestic Heat Pumps," International Journal of Refrigeration, **32**(8), pp. 1918–1928.

[5] Schiffmann, J., Kontomaris, K., Arpagaus, C., Bless, F., and Bertsch, S., 2020, "Scale Limitations of Gas Bearing Supported Turbocompressors for Vapor Compression Cycles," International Journal of Refrigeration, **109**, pp. 92–104.

[6] Demierre, J., Rubino, A., and Schiffmann, J., 2014, "Modeling and Experimental Investigation of an Oil-Free Microcompressor-Turbine Unit for an Organic Rankine Cycle Driven Heat Pump," J. Eng. Gas Turbines Power, **137**(3), pp. 032602–032602.

[7] Cunningham, R. E., Fleming, D. P., and Anderson, W. J., 1971, "Experimental Load Capacity and Power Loss of Herringbone Grooved Gas Lubricated Journal Bearings," J. of Lubrication Tech, **93**(3), pp. 415–422.

[8] Schiffmann, J., 2008, "Integrated Design, Optimization and Experimental Investigation of a Direct Driven Turbocompressor for Domestic Heat Pumps," Ph.D. thesis, Ecole Polytechnique Fédérale de Lausanne.

[9] Allaire, P. E., Kasarda, M. E. F., and Fujita, L. K., 1999, "Rotor Power Losses in Planar Radial Magnetic Bearings—Effects of Number of Stator Poles, Air Gap Thickness, and Magnetic Flux Density," J. Eng. Gas Turbines Power, **121**(4), pp. 691–696.
[10] Kasarda, M. E. F., Allaire, P. E., Norris, P. M., Mastrangelo, C., and Maslen, E. H., 1999, "Experimentally Determined Rotor Power Losses in Homopolar and Heteropolar Magnetic Bearings," J. Eng. Gas Turbines Power, **121**(4), pp. 697–702.
[11] Millward, J. A., and Edwards, M. F., 1996, "Windage Heating of Air Passing Through Labyrinth Seals," J. Turbomach, **118**(2), pp. 414–419.
[12] Massini, D., Fondelli, T., Andreini, A., Facchini, B., Tarchi, L., and Leonardi, F., 2018, "Experimental and Numerical Investigation on Windage Power Losses in High Speed Gears," J. Eng. Gas Turbines Power, **140**(8), pp. 082508-082508–11.
[13] Zwyssig, C., Round, S. D., and Kolar, J. W., 2006, "Analytical and Experimental Investigation of a Low Torque, Ultra-High Speed Drive System," *Conference Record of the 2006 IEEE Industry Applications Conference Forty-First IAS Annual Meeting*, pp. 1507–1513.
[14] Luomi, J., Zwyssig, C., Looser, A., and Kolar, J. W., 2009, "Efficiency Optimization of a 100-W 500 000-r/Min Permanent-Magnet Machine Including Air-Friction Losses," IEEE Transactions on Industry Applications, **45**(4), pp. 1368–1377.
[15] Huynh, C., Zheng, L., and Acharya, D., 2008, "Losses in High Speed Permanent Magnet Machines Used in Microturbine Applications," J. Eng. Gas Turbines Power, **131**(2), pp. 022301-022301–6.
[16] Mack, M., 1967, "Luftreibungsverluste Bei Elektrischen Maschinen Kleiner Baugrösse," Ph.D. Thesis, Universität Stuttgart.
[17] Couette, M. M., 1890, "Etudes Sur Le Frottement Des Liquides," Ann. Chim. Phys., **21**.
[18] Taylor, G. I., 1923, "Stability of a Viscous Liquid Contained between Two Rotating Cylinders," Philos. Trans. Roy. Soc., Lond., **223**.
[19] Nachouane, A. B., Abdelli, A., Friedrich, G., and Vivier, S., 2016, "Estimation of Windage Losses inside Very Narrow Air Gaps of High Speed Electrical Machines without an Internal Ventilation Using CFD Methods," *2016 XXII International Conference on Electrical Machines (ICEM)*, pp. 2704–2710.
[20] Childs, P. R. N., 2011, *Rotating Flow*, Butterworth-Heinemann.
[21] Wendt, F., 1933, "Turbulente Strömungen zwischen zwei rotierenden konaxialen Zylindern," Ing. arch, **4**(6), pp. 577–595.
[22] Yamada, Y., 1962, "Torque Resistance of a Flow between Rotating Co-Axial Cylinders Having Axial Flow," Bulletin of JSME, **5**(20), pp. 634–642.
[23] Vrancik, J. E., 1968, *Prediction of Windage Power Loss in Alternators*, D-4849, NASA Lewis Research Center, Washington DC, USA.
[24] Bilgen, E., and Boulos, R., 1973, "Functional Dependence of Torque Coefficient of Coaxial Cylinders on Gap Width and Reynolds Numbers," J. Fluids Eng, **95**(1), pp. 122–126.
[25] Lathrop, D. P., Fineberg, J., and Swinney, H. L., 1992, "Turbulent Flow between Concentric Rotating Cylinders at Large Reynolds Number," Phys. Rev. Lett., **68**(10), pp. 1515–1518.
[26] Wild, P. M., Djilali, N., and Vickers, G. W., 1996, "Experimental and Computational Assessment of Windage Losses in Rotating Machinery," J. Fluids Eng, **118**(1), pp. 116–122.
[27] Burnand, G., Araujo, D. M., Koechli, C., and Perriard, Y., 2017, "Validation by Measurements of a Windage Losses Model for Very-High-Speed Machines," *2017 20th International Conference on Electrical Machines and Systems (ICEMS)*, pp. 1–4.
[28] Daily, J. W., and Nece, R. E., 1960, "Chamber Dimension Effects on Induced Flow and Frictional Resistance of Enclosed Rotating Disks," J. Basic Eng, **82**(1), pp. 217–230.
[29] Gu, L., Guenat, E., and Schiffmann, J., 2020, "A Review of Grooved Dynamic Gas Bearings," Appl. Mech. Rev, **72**(1).
[30] Hearn, E. J., 1997, *Mechanics of Materials Volume 2*, Butterworth-Heinemann.
[31] Lemmon, E. W., Bell, I. H., Huber, M. L., and McLinden, M. O., 2018, "NIST Standard Reference Database 23: Reference Fluid Thermodynamic and Transport Properties-REFPROP, Version 10.0."